Journal of the Civil Engineering Forum, September 2026, 12(3):403-414
DOI 10.22146/jcef.18862
Available Online at https://jurnal.ugm.ac.id/v3/jcef/issue/archive

Scenario-Neutral Assessment of Rainfall–Erosion Sensitivity Using RUSLE in the Sempor Reservoir Catchment, Indonesia

Irfan Fadillah Widianto, Suroso*, Purwanto Bekti Santoso
Department of Civil Engineering, Universitas Jenderal Soedirman, Purwokerto, INDONESIA
*Corresponding author: surosotsipil@unsoed.ac.id

SUBMITTED 29 December 2024 **REVISED** 5 January 2026 **ACCEPTED** 6 April 2026

ABSTRACT Rainfall variability poses a substantial threat to reservoir sustainability in tropical monsoon catchments because changes in rainfall intensity and seasonality directly influence soil detachment, runoff generation, and sediment–source pressure. Conventional climate–impact assessments commonly rely on a limited number of deterministic climate projections, which may obscure the broader sensitivity of catchment erosion to plausible rainfall changes. This study integrates a scenario–neutral (SN) framework with the Revised Universal Soil Loss Equation (RUSLE) to evaluate rainfall–erosion sensitivity in the Sempor Reservoir catchment, Central Java, Indonesia. Historical daily rainfall was used to establish the baseline, while systematic perturbations of annual precipitation, seasonal rainfall distribution, wet–day frequency, and extreme rainfall intensity were used to construct a broad rainfall–exposure space. Changes in rainfall erosivity were subsequently propagated through RUSLE while soil erodibility, topography, land cover, and support–practice factors were held constant. The resulting estimates represent potential hillslope soil loss and sediment–source pressure rather than direct measurements of sediment delivery or reservoir deposition. The results reveal pronounced seasonal and spatial contrasts. Wet–season rainfall contributes more than 60% of annual rainfall erosivity and approximately 70–80% of annual estimated soil loss. The greatest estimated erosion occurs where relatively high rainfall erosivity coincides with higher soil–erodibility, topographic, cover–management, and support–practice factors. Increasing wet–season rainfall produces a marked increase in estimated soil loss, indicating that erosion sensitivity is influenced by rainfall timing and intensity as well as annual rainfall totals. The scenario–neutral simulations reproduce baseline medians and seasonal patterns consistently but attenuate the upper distribution tails and consequently underrepresent rare extreme events. The integrated SN–RUSLE framework therefore provides a transparent approach for diagnosing rainfall–erosion sensitivity under climate uncertainty. The findings support prioritising wet–season erosion control, maintaining vegetation cover, and implementing spatially targeted conservation measures in areas with higher estimated erosion potential.

KEYWORDS Climate change; RUSLE; Scenario–neutral; Soil erosion; Reservoir sedimentation.

1 INTRODUCTION

Climate change is altering temperature regimes, seasonal precipitation patterns, and the frequency and intensity of extreme rainfall (Yuliana et al., 2024). Projections for Southeast Asia indicate substantial changes in rainfall distribution during the twenty–first century, including an estimated 10–20% increase in extreme precipitation during boreal winter (December–February) and a 10–30% decrease during boreal summer (June–August) (Tangang et al., 2020). Observations across Indonesia show a significant increase in daily rainfall intensity of approximately 0.21 mm d^{-1} per decade during 1983–2013 (Supari et al., 2017). Such changes in rainfall magnitude, intensity, and seasonal distribution can alter runoff generation, flood response, soil detachment, and sediment transport. In addition to long-term climate trends, interannual variability associated with the El Niño–Southern Oscillation (ENSO) may further modulate rainfall extremes and the associated erosion risk in Indonesia (Aldrian and Dwi Susanto, 2003).

Soil erosion is a major environmental consequence of altered rainfall regimes, particularly in tropical monsoon environments (Olii et al., 2026). Globally, water erosion removes an estimated 35.9 billion tonnes of soil annually (Borrelli et al., 2017), threatening soil productivity, food production, and the long–term sustainability of agricultural land (Pimentel and Burgess, 2013). Although only a fraction of eroded soil is transported to downstream water bodies, persistent sediment delivery can progressively reduce reservoir storage and impair reservoir functions. Changes in riverine sediment loads further demonstrate that sediment delivery is controlled by the combined effects of climatic variability and human disturbance within contributing catchments (Walling and Fang, 2003). Sempor Reservoir in Central Java illustrates this problem. Over more than three decades of operation, cumulative sediment accumulation has been estimated at approximately 15 million m^3, and the reservoir's irrigation–service functionality has reportedly declined to approximately 60% of its original level (Budiman and

Suprayogi, 2024). This long–term accumulation may impair reservoir functions, including flood regulation, irrigation, and water supply. High–intensity rainfall and upstream land–use changes, including deforestation and agricultural expansion, may further increase runoff, soil detachment, and sediment mobilisation (Nearing et al., 2004; Vanacker et al., 2007; Haqdad et al., 2025).

Existing RUSLE applications commonly use historical rainfall or a limited set of deterministic climate projections. Such analyses estimate erosion under selected conditions but provide less information about how the catchment responds across a wider range of plausible rainfall changes. This study therefore integrates RUSLE with a scenario–neutral framework that systematically perturbs rainfall characteristics and evaluates the resulting erosion response. The approach retains RUSLE's transparent representation of rainfall, soil, topography, land cover, and conservation practices while shifting the emphasis from prediction to sensitivity assessment. The study addresses three questions: (1) How do spatial variations in RUSLE factors shape baseline soil–loss patterns in the Sempor catchment? (2) How sensitive are rainfall erosivity and estimated soil loss to scenario–neutral changes in rainfall intensity and seasonality? (3) Which seasons and locations should be prioritised for erosion–control measures?

RUSLE is well suited to this purpose because its multiplicative structure makes the effect of changes in rainfall erosivity explicit. Instead of estimating erosion for only a few predefined climate scenarios, the scenario-neutral framework explores a broader exposure space by systematically modifying rainfall attributes. This design enables consistent comparison of erosion responses while retaining the observed spatial distributions of soil erodibility, topography, land cover, and conservation practices.

The framework combines historical rainfall with synthetic perturbations that alter rainfall intensity and seasonal distribution. The resulting changes in the R factor are propagated through RUSLE while the other model factors are held constant. Consequently, the outputs represent sensitivity indicators for potential hillslope soil loss and sediment-source pressure; they are not deterministic future projections, direct measurements of erosion, or estimates of sediment deposited in the reservoir. Accordingly, this study aims to identify when and where the Sempor catchment is most sensitive to rainfall–driven erosion and to translate those findings into priorities for seasonally and spatially targeted watershed conservation.

2 STUDY AREA AND DATA

2.1 Study Area

The Sempor Reservoir catchment is located near Sempor Village, Kebumen Regency, Central Java, at the foothills of the Southern Serayu Mountains. The catchment covers approximately 40.6 km² and has hilly to mountainous terrain. Slopes range from about 15% to more than 50%, and approximately 12% of the catchment exceeds 45%, indicating substantial erosion potential (Budiman and Suprayogi, 2024). Elevations range from 100 to 600 m above sea level. The dominant soils are clay loam and silt loam derived from weathered volcanic material and have moderate to high erodibility. The catchment has a tropical monsoon climate, with maximum monthly rainfall exceeding 400 mm and mean annual rainfall of approximately 2,700 mm. The wet season generally extends from November to March, whereas the drier period occurs from April to October.

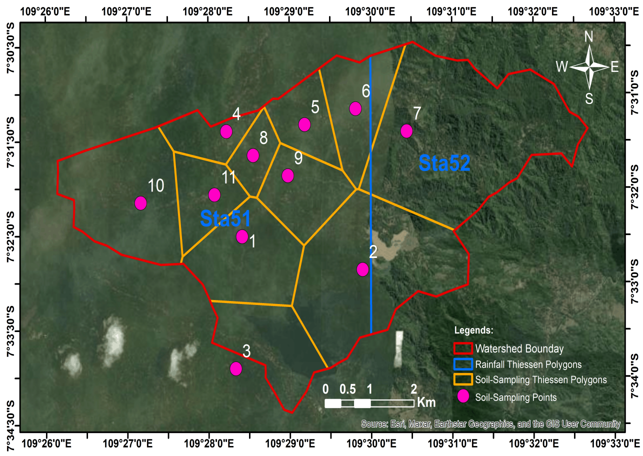

Figure 1. Sempor Reservoir catchment, rainfall stations, and soil–sampling locations. The red line delineates the catchment; yellow lines show the Thiessen polygons; blue labels identify Sta–51 and Sta–52; pink circles mark the soil–sampling sites; and the blue line represents the main river.

Constructed in the 1970s, Sempor Reservoir was initially developed for flood control and subsequently expanded to support irrigation for approximately 6,478 ha of farmland, raw–water supply, domestic use, and limited hydropower generation. The rock–fill embankment dam is equipped with a 26 m–wide ogee spillway with a crest elevation of 136.60 m and a horseshoe–shaped outlet with a maximum discharge capacity of approximately 179.5 $m^3\ s^{-1}$. Over more than three decades of operation, cumulative sediment accumulation has been estimated at approximately 15 million m^3. This long–term sediment accumulation has reduced the operational performance of the reservoir, particularly its irrigation–service functionality (Budiman and Suprayogi, 2024).

Land-use change in the upstream catchment, particularly deforestation for agriculture and settlement, is an important contributor to increased runoff, soil erosion, and reservoir sedimentation. Together with steep terrain and intense monsoon rainfall, these pressures make the Sempor catchment a suitable case for evaluating rainfall–erosion sensitivity. Figure 1 shows the catchment boundary, rainfall data locations, river network, Thiessen polygons, and soil–sampling sites.

2.2 Data

RUSLE requires spatial information on rainfall, soil properties, topography, land cover, and conservation practices. Daily precipitation data from the Global Precipitation Climatology Centre (GPCC) were obtained for 1979–2019 at two grid points covering the Sempor Reservoir catchment. The 1979–2019 data were used to derive the historical rainfall and erosivity characteristics, whereas the common period 1980–2018 was used for direct comparison between the historical baseline and the scenario-neutral simulations. This common comparison period was selected to ensure consistent temporal coverage between the observed and synthetic rainfall series. Topography was represented using the Shuttle Radar Topography Mission (SRTM) digital elevation model at 90 m resolution. Land use and land cover were obtained from the MODIS MCD12Q1 product at 500 m resolution using the International Geosphere–Biosphere Programme classification. Eleven soil samples collected from different slope and land-use settings were analysed for their sand, silt, clay, and organic–carbon contents to estimate the soil–erodibility factor.

3 METHODOLOGY

3.1 Soil Erosion Estimation Using RUSLE

Potential soil loss in the Sempor Reservoir catchment was estimated using the Revised Universal Soil Loss Equation (RUSLE), an empirical model for estimating long–term average sheet and rill erosion as a function of rainfall erosivity, soil erodibility, topography, land cover, and conservation practices (Renard et al., 1997). The multiplicative relationship among these factors is expressed in Equation (1).

$$A = R \times K \times LS \times C \times P \tag{1}$$

In Equation (1), A is the estimated average annual soil loss (t ha^{-1} yr^{-1}), R is the rainfall–erosivity factor, K is the soil–erodibility factor, LS is the combined slope–length and slope-steepness factor, C is the cover–management factor, and P is the support–practice factor.

The five RUSLE factors were developed from the available catchment data. The R factor was derived from 41 years of daily rainfall data (1979–2019) using an empirical approximation suitable for data–limited conditions. The K factor was estimated from laboratory measurements of 11 soil samples distributed across representative slope and land-use settings. The LS factor was calculated from slope and flow accumulation derived from the 90 m SRTM DEM in ArcGIS. The C and P factors were assigned from the MODIS MCD12Q1 land-cover classes and reference values reported in the RUSLE literature (Nearing et al., 2004; Panagos et al., 2015).

Because sub–hourly rainfall data were unavailable, daily precipitation was converted to an average event intensity by assuming a rainfall duration of 4 h. Daily rainfall intensity, I_{daily}, was calculated by dividing daily precipitation, P (mm), by the assumed event duration. The maximum 30–minute intensity, I_{30}, was subsequently approximated using a correction coefficient of 1.3. The empirical kinetic–energy term, E, used in the study was calculated from the estimated daily rainfall intensity using Equation (2).

$$E = 0.29 \times \left(1 - 0.72 \times e^{-0.05 \times I_{\text{daily}}}\right) \tag{2}$$

The resulting empirical energy term was combined with the estimated maximum 30–minute rainfall intensity to calculate the daily erosivity proxy, R_{daily}, as expressed in Equation (3).

$$R_{\text{daily}} = E \times I_{30} \tag{3}$$

In Equation (2) and Equation (3), I_{daily} is the estimated daily rainfall intensity, I_{30} is the approximated maximum 30–minute rainfall intensity, and E is the empirical kinetic–energy term used in the calculation. The annual erosivity proxy was obtained by summing R_{daily} over all days within each year. Because the calculation was derived from daily rather than sub-hourly rainfall observations, R_{daily} and its annual sum should be interpreted as empirical erosivity proxies for comparative sensitivity assessment, not as direct event-scale EI_{30} measurements. Equation (2) and Equation (3) reproduce the calculation applied in the submitted study; no numerical method or result is changed in this copyediting response.

The soil–erodibility factor, K, was estimated from the particle–size distribution, organic–matter content, soil–structure class, and permeability class of the 11 soil samples. Following the empirical formulation of Wischmeier and Smith (1978), as presented by Renard et al. (1997), the K factor was calculated using Equation (4).

$$K = \frac{\left[2.1\times10^{-4}(12-OM)\,M^{1.14}+3.25(S_{\text{str}}-2)+2.5(P_{\text{class}}-3)\right]}{100} \tag{4}$$

In Equation (4), OM is the soil organic–matter content (%); M is the particle–size parameter, calculated as (% silt + % very fine sand) $\times$ (100 − % clay); S_{str} is the soil–structure code; and P_{class} is the soil–permeability class. Soil–texture classes were determined using the USDA soil–texture triangle, while the structure and permeability codes were assigned using field observations and the corresponding classification criteria.

The combined slope–length and slope-steepness factor, LS, was derived from the 90 m SRTM digital elevation model. Slope steepness was calculated from the terrain gradient, while effective slope length was represented using flow accumulation. The spatial LS factor was calculated using the GIS–based formulation presented in Equation (5), adapted from Renard et al. (1997).

$$LS = \left(\frac{\text{Flow Accumulation}\times\text{Cell Size}}{22.13}\right)^{m} \times \left(\frac{\sin(\theta)}{0.0896}\right)^{n} \tag{5}$$

In Equation (5), θ is the slope angle in radians, m is the slope–length exponent, and n is the slope–steepness exponent. In this study, m varied according to the slope gradient, while n was set to 1.3. The resulting LS raster represents the relative influence of slope length and steepness on potential soil loss, with higher values indicating a greater topographic contribution to erosion.

The cover–management factor (C) was assigned to the MODIS MCD12Q1 LULC classes using values reported in the USLE and RUSLE literature for forest, agricultural land, built–up areas, and water bodies (Wischmeier and Smith, 1978; Renard et al., 1997). The support–practice factor (P) represented the relative effect of practices such as contour farming and terracing. Values were assigned from published reference tables according to land use, slope, and the assumed level of conservation practice (Panagos et al., 2015).

Throughout this study, baseline erosion refers to potential soil loss estimated using RUSLE with historical rainfall during the baseline period and the observed spatial distributions of K, LS, C, and P. It does not represent field-measured erosion, catchment sediment yield, sediment delivered to the river network, or sediment deposited in Sempor Reservoir. The baseline serves as a consistent reference against which the effects of scenario–neutral rainfall perturbations are evaluated, while all non–rainfall RUSLE factors are held constant.

3.2 Modelling Rainfall–Pattern Changes

A scenario–neutral (SN) approach was used to investigate how changes in rainfall characteristics affect potential soil loss without relying on a particular emissions pathway or climate–model projection. Historical daily rainfall for the common comparison period of 1980–2018 was processed in R using the foreSIGHT package. Synthetic rainfall series were generated through an inverse stochastic procedure to reproduce prescribed changes in annual rainfall (P_{ann}), monthly rainfall (P_{month}), number of wet days (n_{wet}), and 99$^{\text{th}}$–percentile rainfall intensity (P_{99}). The exposure space included changes of $\pm$20% in annual rainfall and seasonal redistributions representing, among other conditions, wetter wet seasons and drier dry seasons. One–at–a–time and regular–grid experimental designs were used to examine both individual and combined changes in rainfall attributes. Each synthetic rainfall series was converted into daily rainfall erosivity and subsequently combined with the fixed K, LS, C, and P rasters to calculate the corresponding spatial soil–loss response. The resulting simulations describe catchment sensitivity across the selected rainfall–exposure space rather than the probability or timing of a particular future climatic condition.

4 RESULTS AND DISCUSSION

4.1 Soil Erodibility (K) Factor

The USDA textural classification indicates substantial spatial variation in the catchment soils. Loamy sand (LoSa), with approximately 70–90% sand and generally less than 10% clay, occupies extensive areas. Its high permeability promotes rapid infiltration, but its weak particle cohesion can increase detachment under intense rainfall (Wischmeier and Smith, 1978; Renard et al., 1997). Silty clay (SiCl) contains larger silt and clay fractions and generally has stronger cohesion and aggregate stability. These textural differences influence infiltration, water retention, runoff generation, and erodibility (Lal, 2001).

High M values (typically >3,500) indicate a large proportion of silt and very fine sand relative to clay. These particles are readily detached by raindrop impact and runoff, whereas a larger clay fraction generally increases cohesion and aggregate stability (Lal, 2001; Panagos et al., 2015). The mapped areas with high M values are therefore more susceptible to erosion, especially under intense rainfall. This interpretation is consistent with the RUSLE erodibility formulation (Renard et al., 1997) and supports prioritising protective measures such as mulch and continuous vegetation cover.

Measured organic carbon ranges from 0.28% to 1.96% (Table 1), with the highest values occurring in loam

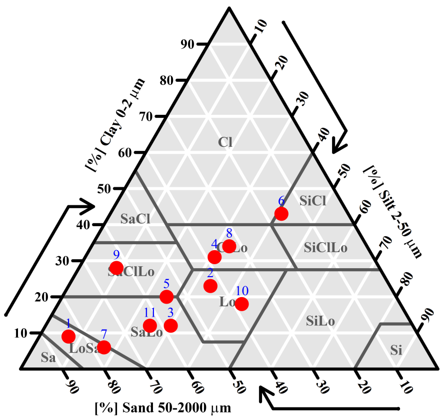

Figure 2. USDA soil–texture classification of samples from the Sempor catchment. Red points show the 11 samples plotted by their sand (50–2,000 μm), silt (2–50 μm), and clay (<2 μm) fractions. Abbreviations identify the corresponding USDA texture classes.

samples. Higher organic–carbon content generally improves aggregation, water retention, and resistance to detachment (Wischmeier and Smith, 1978; Renard et al., 1997). Areas with low organic carbon may therefore benefit from organic amendments and residue management, although site–specific agronomic assessment is required. This interpretation is consistent with the relationship between soil carbon and aggregate stability reported by Hassink et al. (1997).

Mapped soil–structure scores range from 2.25 to 3.00 on the categorical scale used in the K–factor calculation. Higher scores represent more granular and stable structures, whereas lower scores represent less aggregated, more massive structures. Well–aggregated soil promotes macropore formation and infiltration and is more resistant to raindrop detachment; poorly aggregated soil is more likely to generate surface runoff. Soil structure therefore affects both agricultural function and erosion resistance (Dexter, 2004).

Soil–permeability classes range from 2 (moderately slow) to 4 (moderately rapid) on the USDA scale of 1 (very slow) to 6 (very rapid). These classes represent relative rates of water movement through the soil and were assigned from field observations of texture and structure. Loamy sand generally has higher permeability and lower water retention, whereas less permeable areas are more likely to generate surface runoff. Permeability is therefore an important control on catchment water regulation and erosion susceptibility (Zhang et al., 2004).

The calculated K factor ranges from 0.15 to 0.25; higher values occur in soils with greater silt and fine–sand content, whereas lower values are associated with more clay and organic carbon. Figure 2 shows the USDA textural classification of the samples Table 1 summarises their particle–size composition and organic–carbon content, and Figure 3 presents the spatial distributions of the K–factor inputs and the resulting erodibility values. These patterns are consistent with the greater detachment susceptibility of silt– and fine–sand–rich soils (Wischmeier and Smith, 1978).

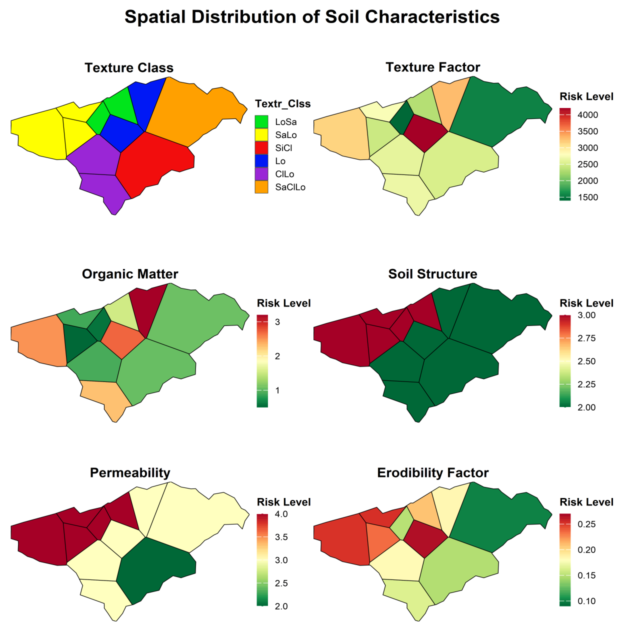

Figure 3. Spatial distribution of soil properties and the K factor in the Sempor catchment. The panels show texture class, texture–related erodibility, organic matter, soil structure, permeability, and the resulting erodibility factor. Red indicates relatively high values or susceptibility and green indicates relatively low values.

4.2 Slope Length and Steepness (LS), Cover–Management (C), and Support–Practice (P) Factors

Slopes in the Sempor Reservoir catchment range from nearly level to more than 40°. Areas with slopes below 10°, concentrated in valleys and lowlands, cover approximately 41.7% of the catchment and generally have lower topographic erosion potential. Slopes steeper than 30°, located mainly in upstream hills and ridge zones, occupy approximately 26.4% and have substantially greater erosion potential. The catchment therefore contains extensive areas of moderate to high topographic susceptibility, particularly on long, steep hillslopes.

Slope controls runoff velocity and sediment–transport capacity; steeper terrain increases the energy available for soil detachment and downslope transport (Morgan, 2005). The flow–direction map shows drainage convergence towards valleys connected to the reservoir, while the flow–accumulation map identifies preferential runoff and sediment pathways. Cells with accumulation values above 250 are concentrated along

Table 1. Soil–texture classification, particle–size composition, and organic–carbon content of the 11 samples

No	Texture Class	Description	Sand (%)	Silt (%)	Clay (%)	Organic C (%)
1	LoSa	Loamy sand: predominantly sandy, with little silt and clay; high permeability.	84	7	9	0.38
2	Lo	Loam: a balanced mixture of sand, silt, and clay with generally favourable physical properties.	43	34	23	1.96
3	SaLo	Sandy loam: sand-dominated soil with smaller silt and clay fractions; moderately high permeability.	58	30	12	1.67
4	ClLo	Clay loam: substantial clay with comparable sand and silt fractions; good water retention and moderate permeability.	38	31	31	1.33
5	SaLo	Sandy loam: sand-dominated soil with smaller silt and clay fractions; moderately high permeability.	55	25	20	0.28
6	SiCl	Silty clay: high silt and clay content; generally low permeability.	16	41	43	0.61
7	LoSa	Loamy sand: predominantly sandy, with little silt and clay; high permeability.	77	17	6	1.02
8	ClLo	Clay loam: substantial clay with comparable sand and silt fractions; good water retention and moderate permeability.	33	33	34	0.53
9	SaClLo	Sandy clay loam: sand-dominated soil with a substantial clay fraction and moderate water retention.	63	9	28	0.62
10	Lo	Loam: a balanced mixture of sand, silt, and clay with generally favourable physical properties.	38	44	18	1.57
11	SaLo	Sandy loam: sand-dominated soil with smaller silt and clay fractions; moderately high permeability.	63	25	12	0.59

the main drainage network and may be susceptible to concentrated–flow erosion. These locations are suitable priorities for field verification and measures such as vegetative buffers, check dams, or sediment barriers (Moore et al., 1991; Renard et al., 1997).

The LS factor ranges from 0 to more than 6. High values occur on long, steep slopes and indicate strong topographic control on erosion; areas with LS >5 therefore warrant priority consideration for slope stabilisation and soil–cover measures (Wischmeier and Smith, 1978). The C factor ranges from 0 for water bodies to 0.2 for agricultural land, with higher values indicating less protective cover. The P factor ranges from 0.6, representing more effective support practices, to 1.0, representing no assumed erosion–reducing practice. Locations where high LS, C, and P values coincide have the greatest management priority.Trimble and Crosson (2000) emphasize that reducing P values through effective conservation can significantly minimize soil erosion. Figure 4 shows the topographic and RUSLE–factor maps.

4.3 Rainfall Erosivity (R) Factor

The R factor represents the erosive potential of rainfall and is strongly seasonal at both locations, with pronounced variability across daily, monthly, and annual time scales (Figure 5). Daily erosivity ranges from approximately 0 to 20 MJ mm ha^{-1} h^{-1} at both stations. Median values are highest in January, at about 10 MJ mm ha^{-1} h^{-1}for Sta-51 and 12 MJ mm ha^{-1} h^{-1} for Sta–52 and fall below 2 MJ mm ha^{-1} h^{-1} in August. This contrast confirms that wet–season rainfall contributes disproportionately to erosive energy (Renard et al., 1997).

At the monthly scale, erosivity reaches its highest levels in December and January, averaging approximately 40–50 MJ mm ha^{-1} h^{-1} at Sta–51 and 45–55 MJ mm ha^{-1} h^{-1} at Sta–52. August and September have the lowest values, generally 5–10 MJ mm ha^{-1} h^{-1}. The strong month–to–month contrast reflects the seasonal concentration of high–intensity rainfall and is consistent with the sensitivity of erosion to rainfall variability described by Nearing et al. (2004).

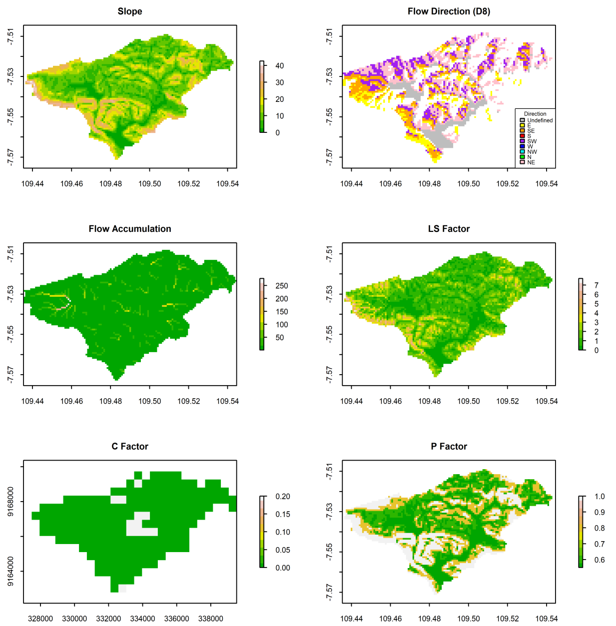

Figure 4. Spatial distribution of topographic and RUSLE factors in the Sempor catchment. The panels show slope, D8 flow direction, flow accumulation, LS, C, and P. Higher LS and C values indicate greater erosion susceptibility, whereas lower P values represent more effective support practices.

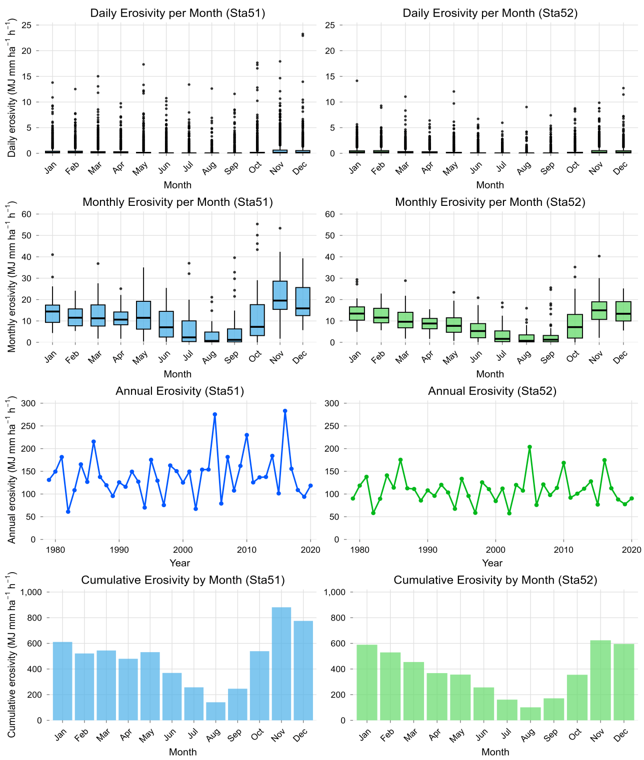

Figure 5. Temporal variation in rainfall erosivity at Sta–51 and Sta–52. The top two rows show daily and monthly distributions by month; the third row shows annual variation; and the bottom row shows cumulative monthly erosivity. Erosivity is concentrated from November to March.

Annual erosivity ranges from approximately 70 to 120 MJ mm ha^{-1} h^{-1} at Sta–51 and 80 to 130 MJ mm ha^{-1} h^{-1} at Sta–52 over the period shown. No clear monotonic trend is visually evident, although marked peaks occur in several years, including 1983, 1997, and 2010. These peaks demonstrate strong interannual variability; possibly associated with ENSO (El Niño–Southern Oscillation). Previous studies showed that El Niño increases rainfall intensity in certain tropical regions, elevating soil erosion risks (Pruski and Nearing, 2002).

Cumulative monthly erosivity is highest in January, reaching approximately 750 MJ mm ha^{-1} at Sta–51 and more than 800 MJ mm ha^{-1} at Sta–52, and lowest in September, at about 100 MJ mm ha^{-1} at both stations. Differences between the two locations may reflect spatial variability in the gridded rainfall input; confirmation of local topographic or microclimatic controls would require additional rain–gauge observations.

The wet season (December–February) contributes more than 60% of annual rainfall erosivity, whereas June–September contributes less than 20%. This concentration identifies the wet season as the critical period for erosion-control measures. The result is specific to the Sempor catchment and provides the temporal basis for the subsequent scenario–neutral sensitivity analysis.

4.4 Soil Erosion Rates

The daily soil–loss distributions show a clear seasonal cycle. Median daily erosion peaks from January to March at approximately 0.08 t ha^{-1} d^{-1} for Sta–51 and 0.09 t ha^{-1} d^{-1} for Sta–52. The highest value at Sta–52 is approximately 0.15 t ha^{-1} d^{-1} in January. From June to September, median daily erosion approaches zero at both locations because rainfall erosivity is low. This pattern is consistent with the direct influence of rainfall energy on RUSLE–estimated soil loss (Nearing et al., 2004).

Monthly erosion is highest in December and January, with median values of approximately 0.3 t ha^{-1} month^{-1} at Sta–51 and 0.4 t ha^{-1} month^{-1} at Sta–52. December totals reach about 4.5 t ha^{-1} at Sta–51 and 6 t ha^{-1} at Sta–52, whereas July–September values are generally below 0.5 t ha^{-1}. Approximately 70–80% of the annual estimated soil loss occurs from December to March, confirming the dominance of wet-season rainfall (Lu et al., 2006).

Annual RUSLE–estimated soil loss averages approximately 1.2 t ha^{-1} yr^{-1} at Sta–51 and 1.7 t ha^{-1} yr^{-1} at Sta–52. Values range from about 0.5 to 2.0 t ha^{-1} yr^{-1} at Sta–51 and reach approximately 2.5 t ha^{-1} yr^{-1} at Sta–52 in high-erosivity years such as 1997 and 2010.

Because R is the only time–varying RUSLE factor in this analysis, the interannual erosion peaks directly track rainfall erosivity; they should not be interpreted as independently observed erosion events.

Sta–52 produces consistently higher erosion estimates than Sta–51. This difference is consistent with the steeper terrain associated with the Sta–52 area, where slopes commonly reach 25–40%, compared with approximately 10–20% around Sta–51, and with median monthly erosivity that is about 15–20% higher. The combined effects of larger LS and R factors therefore explain the higher RUSLE estimates at Sta–52 (Renard et al., 1997). Figure 6 presents the daily, monthly, and annual patterns.

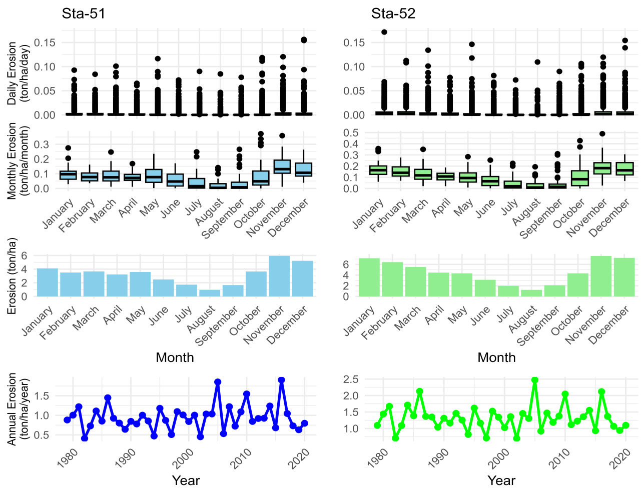

Figure 6. Daily, monthly, and annual RUSLE–estimated soil loss at Sta–51 and Sta–52. The upper and middle rows show monthly distributions of daily and monthly estimates, and the lower row shows annual variation. In this figure, “observed” denotes the baseline RUSLE calculation driven by historical rainfall, not field–measured erosion.

4.5 Scenario–Neutral Rainfall Perturbations

The historical mean precipitation, selected perturbation multiplier, and scenario–adjusted values for Sta–51 and Sta–52 define sensitivity points within the scenario–neutral exposure space rather than observed trends or probabilistic climate projections (Table 2). For the selected annual perturbation, mean precipitation at Sta–51 increases from 2,812 to 3,056 mm (multiplier 1.09), while Sta–52 increases from 2,453 to 2,551 mm (multiplier 1.04). This configuration imposes a larger annual rainfall change at Sta–51 and is used to examine how different rainfall perturbations propagate through the erosion model.

The monthly perturbations vary by season. In January, precipitation at Sta–51 increases from 308 to 391 mm (multiplier 1.27), and February increases from 262 to 342 mm (1.30). At Sta–52, the corresponding multipliers are 1.26 and 1.32. These wet–season perturbations test the catchment response to more intense rainfall during months that already have high baseline erosivity. May, June, and July are assigned lower precipitation at both locations. For example, May precipitation at Sta–51 decreases from 227 to 181 mm (multiplier 0.80), while Sta–52 decreases from 180 to 158 mm (0.88). These perturbations represent drier dry–season conditions and allow their effects on seasonal erosion estimates to be evaluated. At Sta–51, August precipitation increases from 71 to 140 mm (multiplier 1.97) and September from 111 to 218 mm (1.96). The corresponding changes at Sta–52 are smaller, with multipliers of 1.16 and 1.10. These scenarios explore sensitivity to a wetter late dry season; they should not be interpreted as evidence that the rainy season has already lengthened.

The perturbations span wetter and drier conditions across the year and reveal how the timing of rainfall change affects estimated erosion. Increases during already wet months are expected to produce the largest soil–loss response, especially on steep and poorly protected slopes, whereas drier scenarios primarily reduce erosivity. The results are therefore most useful for identifying sensitivity and management priorities rather than forecasting a single future condition.

The exposure–space analysis supports data-driven mitigation by linking seasonal rainfall perturbations to spatial erosion hotspots. Conservation planning should prioritise locations where steep slopes, erodible soils, limited cover, and high wet-season erosivity coincide.

Historical precipitation is compared with the scenario–neutral synthetic series at daily and monthly scales for Sta–51 and Sta–52 (Figure 7). However, it should be noted that this comparison is intended only as a diagnostic check of how well the synthetic series preserve relevant characteristics of the historical rainfall distribution and does not constitute a predictive validation of future rainfall. At the daily scale, simulated medians are close to the historical medians in most months, particularly from December to March. The synthetic series nevertheless has a narrower upper tail. At Sta–51 in December, for example, the historical upper range reaches approximately 50 mm, whereas the simulated range is closer to 40 mm. The scenario–neutral approach therefore reproduces central behaviour more consistently than rare high-intensity events (e.g., Bennett et al. 2021).

The monthly comparison reveals generally strong agreement between the historical and synthetic precipitation series, particularly during the wet season. For instance, historical monthly precipitation in December is approximately 400 mm at Sta–51 and 380 mm at Sta–52, compared with about 390 and 370 mm, respectively, in the synthetic series. These small differences

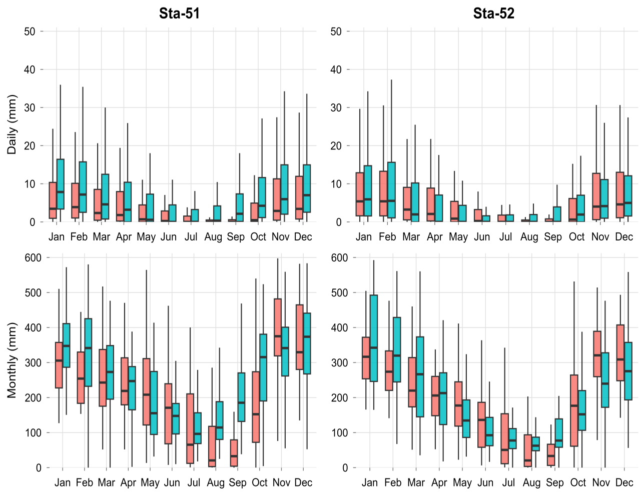

Figure 7. Historical and scenario–neutral daily and monthly precipitation at Sta–51 and Sta–52. Red boxplots show the historical record and blue boxplots show the synthetic series. Boxes represent the interquartile range and median; whiskers and points show the remaining spread and outliers.

indicate that the simulations preserve the dominant monthly rainfall pattern, although some dry–season bias remains. This behaviour is consistent with findings reported by Guo et al. (2017), who noted improved performance of scenario–neutral models at longer temporal scales. This agreement remains evident from November to March, when monthly median precipitation generally ranges from 300 to 500 mm. However, some dry–season bias persists, especially at Sta–51 during June–September, when the synthetic series is frequently lower than the historical record; for example, the July values are approximately 100 mm and 120 mm, respectively. Further calibration may therefore be required when accurately representing low–rainfall conditions is important.

Rainfall distributions indicate greater wet–season variability at Sta–52 than at Sta–51, particularly during peak rainfall months. In December, the upper range of the historical distribution reaches approximately 600 mm at Sta–52 and 500 mm at Sta–51. This contrast may reflect spatial variability in the gridded rainfall data, but attribution to orographic effects requires local gauge observations.

The synthetic series performs best in high–rainfall months, when daily and monthly medians generally differ from the historical values by less than 5%. Performance is weaker in the distribution tails and in some dry months. In August at Sta–51, for example, simulated monthly precipitation is approximately 70 mm compared with about 50 mm in the historical record. The scenario–neutral series therefore provides a suitable representation of median, monthly, and seasonal rainfall behaviour for the intended sensitivity analysis. Its tendency to attenuate extremes and its dry-season biases should be considered when interpreting the erosion response. Applications focused on rare events would require additional observations or a stochastic model specifically calibrated to the distribution tails.

4.6 Scenario–Neutral Assessment of Soil–Erosion Sensitivity

Baseline RUSLE soil–loss estimates, calculated using historical rainfall and observed catchment factors, are compared with estimates generated from the scenario–neutral rainfall series at Sta–51 and Sta–52 (Figure 8). Because neither dataset represents field measurements of erosion, this comparison evaluates consistency and sensitivity rather than predictive accuracy. At the daily scale, the scenario–neutral closely follows the baseline distributions. Median values range from approximately 0.02 to 0.10 t ha^{-1} d^{-1} at Sta–51 and from 0.02 to 0.15 t ha^{-1} d^{-1} at Sta–52. This agreement shows that the synthetic rainfall series preserves the dominant daily erosion response. Agreement is even stronger at the monthly scale. Baseline December erosion is approximately 8 t ha^{-1} $month^{-1}$ at Sta–51 and nearly 15 t ha^{-1} $month^{-1}$ at Sta–52, compared with about 7 and 13 t ha^{-1} $month^{-1}$, respectively, for the scenario–neutral series. Despite these differences, both datasets exhibit the same seasonal pattern, with low erosion during June–September, generally below 2 t ha^{-1} $month^{-1}$, followed by a sharp increase from October to February as rainfall erosivity rises. This consistent seasonal contrast indicates that the wet season dominates the catchment erosion response and should therefore be prioritized in erosion-control planning.

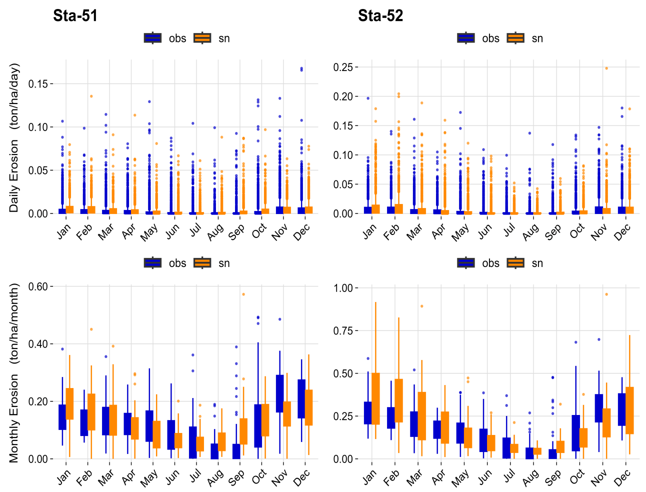

Figure 8. Baseline and scenario–neutral daily and monthly soil–loss estimates at Sta–51 and Sta–52. Blue boxplots ("obs") show the baseline RUSLE estimates driven by historical rainfall, and orange boxplots ("sn") show estimates driven by the synthetic rainfall series. Neither series represents field–measured erosion.

The scenario–neutral series produces slightly lower erosion estimates than the baseline, particularly dur-

Table 2. Historical means, perturbation multipliers, and scenario–adjusted precipitation at Sta–51 and Sta–52 (1980–2018)

Attributes	Sta-51			Sta-52		
	Baseline	Multiplier	Adjusted	Baseline	Multiplier	Adjusted
Annual mean total precipitation (mm)	2812	1.09	3056	2453	1.04	2551
January mean total precipitation (mm)	308	1.27	391	320	1.26	402
February mean total precipitation (mm)	262	1.30	342	286	1.32	377
March mean total precipitation (mm)	263	1.10	288	244	1.18	288
April mean total precipitation (mm)	241	1.00	241	205	0.98	201
May mean total precipitation (mm)	227	0.80	181	180	0.88	158
June mean total precipitation (mm)	176	0.84	147	140	0.82	115
July mean total precipitation (mm)	129	0.92	118	94	0.85	81
August mean total precipitation (mm)	71	1.97	140	57	1.16	66
September mean total precipitation (mm)	111	1.96	218	89	1.10	97
October mean total precipitation (mm)	252	1.14	288	195	0.87	170
November mean total precipitation (mm)	400	0.82	328	324	0.82	264
December mean total precipitation (mm)	373	1.00	374	319	1.04	331

ing the wet season and at the upper end of the distribution. Wet–season medians decrease from approximately 0.10 to 0.08 t ha^{-1} at Sta–51 and from 0.15 to 0.12 t ha^{-1} at Sta–52, whereas median values remain below approximately 0.05 t ha^{-1} in both datasets during the dry months (Figure 9). The attenuation is more pronounced under extreme conditions; for example, at Sta–52 in December, baseline daily outliers reach approximately 0.25 t ha^{-1} d^{-1}, compared with a scenario–neutral maximum of about 0.18 t ha^{-1} d^{-1}. This difference reflects the narrower upper tail of the synthetic rainfall distribution, which limits its suitability for extreme–event analysis but does not prevent its use in evaluating median and seasonal erosion sensitivity.

Overall, the scenario–neutral framework reproduces the central and seasonal behaviour of the baseline RUSLE estimates while deliberately exploring rainfall perturbations across a broader exposure space. Its main value is to identify relative sensitivity and conservation priorities, particularly for wet–season erosion in data–limited reservoir catchments. It should not be used as a substitute for event–scale erosion monitoring or direct sediment–yield measurements.

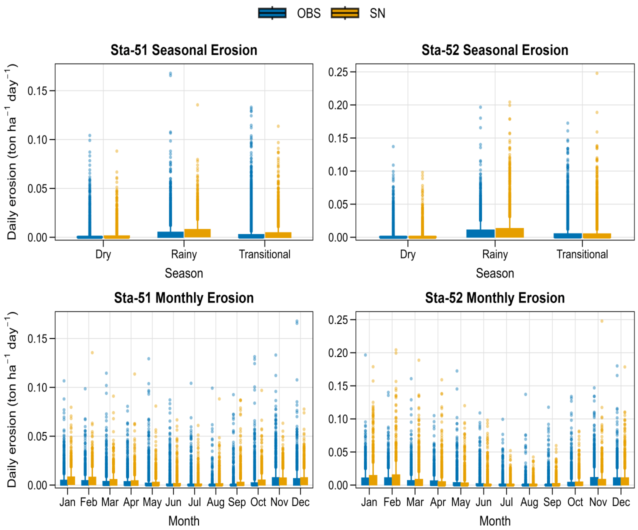

Figure 9. Baseline and scenario–neutral soil–loss estimates by season and month at Sta–51 and Sta–52. Blue boxplots (“obs”) show baseline RUSLE estimates, and orange boxplots (“sn”) show scenario–neutral estimates. The comparison evaluates seasonal and monthly consistency; neither series represents field–measured erosion.

5 CONCLUSION

Integrating a scenario–neutral rainfall framework with RUSLE provides a transparent method for assessing rainfall–erosion sensitivity in the Sempor Reservoir catchment. The analysis treats RUSLE outputs as estimates of potential hillslope soil loss and sediment–source pressure, not as direct observations of erosion, sediment delivery, or reservoir deposition. The baseline results show strong seasonality. Wet–season rainfall contributes more than 60% of annual erosivity and approximately 70–80% of annual estimated soil loss. Median wet–season erosion reaches about 0.10 t h^{-1} at Sta–51 and 0.15 t h^{-1} at Sta–52, with consistently higher values at Sta–52 because of its larger rainfall–erosivity and topographic factors.

The scenario–neutral simulations reproduce monthly and seasonal medians well but generally attenuate the upper tails. Peak monthly erosion is therefore slightly lower than the baseline, and rare daily extremes are underrepresented. The framework is consequently appropriate for sensitivity assessment and comparison of seasonal responses, but not for detailed prediction of extreme events. The results support prioritising erosion–control measures before and during the wet season, particularly where high LS, K, C, and P values overlap. Continuous vegetation cover, contour-based practices, slope stabilisation, and sediment–control structures should be targeted to these hotspots and verified through field assessment.

Further work should reconcile the rainfall periods used in the different analyses, validate the daily erosivity approximation with sub–daily gauge data, calibrate the stochastic rainfall generator for distribution tails, and compare RUSLE estimates with measured sediment yield or reservoir surveys. These steps are necessary before the framework can be used for quantitative forecasting or sedimentation assessment.

DISCLAIMER

The authors declare no conflict of interest.

ACKNOWLEDGMENTS

The authors gratefully acknowledge financial support from the Ministry of Research, Technology, and Higher Education of the Republic of Indonesia through the PTM–DIKTI scheme.

REFERENCES

Aldrian, E. and Dwi Susanto, R. (2003), ‘Identification of three dominant rainfall regions within indonesia and their relationship to sea surface temperature’, *International Journal of Climatology* **23**(12), 1435–1452.
URL: *https://doi.org/10.1002/joc.950*

Bennett, G., Bussi, G., Whitehead, P. G., Bowes, M. J., Read, D. S. and Collins, A. L. (2021), ‘Evaluating impacts of climate change on river sediment dynamics in the uk: A modelling approach’, *Environmental Research Letters* **16**(9), 094014.
URL: *https://doi.org/10.1088/1748-9326/ac1a89*

Borrelli, P., Robinson, D. A., Panagos, P., Lugato, E., Yang, J. E., Alewell, C. and Montanarella, L. (2017), ‘Land use and climate change impacts on global soil erosion by water (2015–2070)’, *Proceedings of the National Academy of Sciences* **114**(36), 9707–9712.
URL: *https://doi.org/10.1073/pnas.1707936114*

Budiman, S. and Suprayogi, S. (2024), ‘Estimating the useful life of the sempor reservoir using erosion modelling’, *Quaestiones Geographicae* **43**(1), 63–78.
URL: *https://doi.org/10.14746/quageo-2024-0004*

Dexter, A. R. (2004), ‘Soil physical quality: Part i. theory, effects of soil texture, density, and organic matter, and effects on root growth’, *Geoderma* **120**(3–4), 201–214.
URL: *https://doi.org/10.1016/j.geoderma.2003.09.004*

Guo, W., Wang, L., Wang, J., Bai, X. and Zhang, S. (2017), ‘Impacts of extreme precipitation events on soil erosion and the effectiveness of vegetation in soil conservation’, *Hydrological Processes* **31**(18), 3284–3296.
URL: *https://doi.org/10.1002/hyp.11260*

Haqdad, K. M. T., Satofuka, Y., Fujimoto, M. and Murata, M. (2025), ‘Impact of tree canopy elevation on rainfall attenuation and soil erosion dynamics for enhanced erosion control’, *Journal of the Civil Engineering Forum* **11**(3), 267–274.
URL: *https://doi.org/10.22146/jcef.18539*

Hassink, J., Bouma, J. and van Noordwijk, M. (1997), ‘Interrelationships between texture, organic carbon storage, macroaggregation, and sustainability of management practices in tropical soils’, *Soil Science Society of America Journal* **61**(5), 1061–1067.
URL: *https://doi.org/10.2136/sssaj1997.03615995006100050006x*

Lal, R. (2001), ‘Soil degradation by erosion’, *Land Degradation & Development* **12**(6), 519–539.
URL: *https://doi.org/10.1002/ldr.472*

Lu, H., Moran, C. J. and Prosser, I. P. (2006), ‘Modelling sediment delivery ratio over the murray darling basin’, *Environmental Modelling & Software* **21**(9), 1297–1308.
URL: *https://doi.org/10.1016/j.envsoft.2005.04.021*

Moore, I. D., Grayson, R. B. and Ladson, A. R. (1991), ‘Digital terrain modelling: A review of hydrological, geomorphological, and biological applications’, *Hydrological Processes* **5**(1), 3–30.
URL: *https://doi.org/10.1002/hyp.3360050103*

Morgan, R. P. C. (2005), *Soil Erosion and Conservation*, 3rd edn, Blackwell Publishing, Oxford.

Nearing, M. A., Pruski, F. F. and O’Neal, M. R. (2004), ‘Expected climate change impacts on soil erosion rates: A review’, *Journal of Soil and Water Conservation* **59**(1), 43–50.
URL: *https://www.jswconline.org/content/59/1/43*

Olii, M. R., Mokarram, M., Anshari, E., Olii, R. S. N. and Pakaya, R. (2026), ‘Machine learning approaches to soil erosion risk mapping: A comparison between logistic regression and fast large margin’, *Journal of the Civil Engineering Forum* **12**(2), 267–280.
URL: *https://doi.org/10.22146/jcef.24796*

Panagos, P., Borrelli, P., Meusburger, K., Alewell, C., Lugato, E. and Montanarella, L. (2015), 'Estimating the soil erosion cover-management factor at european scale', *Land Use Policy* **48**, 38–50.
URL: *https://doi.org/10.1016/j.landusepol.2015.05.021*

Pimentel, D. and Burgess, M. (2013), 'Soil erosion threatens food production', *Agriculture* **3**(3), 443–463.
URL: *https://doi.org/10.3390/agriculture3030443*

Pruski, F. F. and Nearing, M. A. (2002), 'Runoff and soil-loss responses to changes in precipitation: A computer simulation study', *Journal of Soil and Water Conservation* **57**(1), 7–16.
URL: *https://www.jswconline.org/content/57/1/7*

Renard, K. G., Foster, G. R., Weesies, G. A., McCool, D. K. and Yoder, D. C. (1997), *Predicting Soil Erosion by Water: A Guide to Conservation Planning with the Revised Universal Soil Loss Equation (RUSLE)*, Vol. 703 of *Agricultural Handbook*, USDA.

Supari, S., Tangang, F., Juneng, L. and Aldrian, E. (2017), 'Observed trends and projected changes in rainfall characteristics over indonesia based on daily rainfall data', *International Journal of Climatology* **37**(4), 1979–1990.
URL: *https://doi.org/10.1002/joc.4829*

Tangang, F., Chung, J. X., Juneng, L., Supari, Salimun, E., Ngai, S. T., Jamaluddin, A. F., Mohd, M. S. F., Cruz, F., Narisma, G., Santisirisomboon, J., Ngo-Duc, T., Tan, P. V., Singhruck, P., Gunawan, D., Aldrian, E., Sopaheluwakan, A., Nikulin, G., Remedio, A. R. C., Sein, D. V., Hein-Griggs, D., McGregor, J. L., Yang, H., Sasaki, H. and Kumar, P. (2020), 'Projected future changes in rainfall in southeast asia based on cordex–sea multi-model simulations', *Climate Dynamics* **55**, 1247–1267.
URL: *https://doi.org/10.1007/s00382-020-05322-2*

Trimble, S. W. and Crosson, P. (2000), 'U.S. soil erosion rates—myth and reality', *Science* **289**(5477), 248–250.
URL: *https://doi.org/10.1126/science.289.5477.248*

Vanacker, V., von Blanckenburg, F., Govers, G., Barrios, M. and Poortinga, A. (2007), 'Restoring ecosystem functioning in degraded lands', *Science* **315**(5819), 557–558.
URL: *https://doi.org/10.1126/science.1139563*

Walling, D. E. and Fang, D. (2003), 'Recent trends in the suspended sediment loads of the world's rivers', *Global and Planetary Change* **39**(1–2), 111–126.
URL: *https://doi.org/10.1016/S0921-8181(03)00020-1*

Wischmeier, W. H. and Smith, D. D. (1978), *Predicting Rainfall Erosion Losses: A Guide to Conservation Planning*, Vol. 537 of *Agricultural Handbook*, USDA.
URL: *https://naldc.nal.usda.gov/catalog/CAT79706928*

Yuliana, A., Sujono, J. and Karlina (2024), 'Analysis of extreme rainfall in the mt. merapi area', *Journal of the Civil Engineering Forum* **10**(1), 73–84.
URL: *https://doi.org/10.22146/jcef.10084*

Zhang, X. C., Nearing, M. A., Garbrecht, J. D. and Steiner, J. L. (2004), 'Downscaling monthly forecasts to simulate impacts of climate change on soil erosion and wheat production', *Soil Science Society of America Journal* **68**(4), 1376–1385.
URL: *https://doi.org/10.2136/sssaj2004.1376*